

See discussions, stats, and author profiles for this publication at: <https://www.researchgate.net/publication/259572837>

# Polymorphism in Photoluminescent KNdW<sub>2</sub>O<sub>8</sub>: Synthesis, Neutron Diffraction and Raman Study

ARTICLE in CRYSTAL GROWTH & DESIGN · JANUARY 2014

Impact Factor: 4.89 · DOI: 10.1021/cg4017068

CITATION

1

READS

65

6 AUTHORS, INCLUDING:



Swetha S M

Indian Institute Of Science Education and Res...

5 PUBLICATIONS 11 CITATIONS

SEE PROFILE



Chandrabhas Narayana

Jawaharlal Nehru Centre for Advanced Scienti...

155 PUBLICATIONS 1,719 CITATIONS

SEE PROFILE



Joerg Neufeind

Oak Ridge National Laboratory

131 PUBLICATIONS 2,522 CITATIONS

SEE PROFILE



Nalini Sundaram

Poornaprajna Institute of Scientific Research

25 PUBLICATIONS 334 CITATIONS

SEE PROFILE

# Polymorphism in Photoluminescent $\text{KNdW}_2\text{O}_8$ : Synthesis, Neutron Diffraction, and Raman Study

Swetha S. M. Bhat,<sup>†</sup> Diptikanta Swain,<sup>‡</sup> Chandrabhas Narayana,<sup>‡</sup> Mikhail Feygenson,<sup>§</sup> Joerg C. Neufeind,<sup>§</sup> and Nalini G. Sundaram<sup>\*,†</sup>

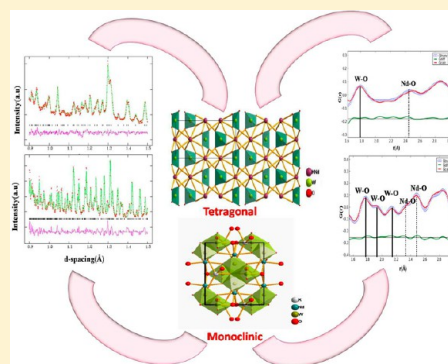
<sup>†</sup>Materials Science Division, Poornaprajna Institute of Scientific Research, Bidalur Near Devanahalli, Bengaluru, Karnataka, India

<sup>‡</sup>CPMU, Jawaharlal Nehru Centre for Advanced Scientific Research, Jakkur, Bengaluru, Karnataka, India

<sup>§</sup>Chemical and Engineering Materials Division, Oak Ridge National Laboratory, Oak Ridge, Tennessee 37831, United States

## S Supporting Information

**ABSTRACT:** Polymorphs of  $\text{KNdW}_2\text{O}_8$  ( $\alpha$ - $\text{KNdW}_2\text{O}_8$  and  $\beta$ - $\text{KNdW}_2\text{O}_8$ ) phosphors were synthesized by an efficient solution combustion technique for the first time. The crystal structure of the polymorphs analyzed from Rietveld refinement of neutron diffraction data confirms that  $\alpha$ - $\text{KNdW}_2\text{O}_8$  crystallizes in the tetragonal system (space group  $I4_1$ ), and  $\beta$ - $\text{KNdW}_2\text{O}_8$  crystallizes in the monoclinic system (space group  $C2/m$ ). The local structure of both polymorphs was elucidated using combined neutron pair distribution function (PDF) and Raman scattering techniques. Photoluminescence measurements of the polymorphs showed broadened emission line width and increased intensity for  $\beta$ - $\text{KNdW}_2\text{O}_8$  in the visible region compared to  $\alpha$ - $\text{KNdW}_2\text{O}_8$ . This phenomenon is attributed to the increased distortion in the coordination environment of the luminescing  $\text{Nd}^{3+}$  ion. Combined PDF, Rietveld, and Raman measurements reveal distortions of the  $\text{WO}_6$  octahedra and  $\text{NdO}_8$  polyhedra in  $\beta$ - $\text{KNdW}_2\text{O}_8$ . This crystal structure–photoluminescence study suggests that this class of tungstates can be exploited for visible light emitting devices by tuning the crystal symmetry.



## 1. INTRODUCTION

Photoluminescent materials have drawn much attention in recent years, due to their potential applications in optoelectronics. The alkali metal double tungstate materials with general formula  $\text{AR}(\text{WO}_4)_2$  ( $\text{A} = \text{Li}^+, \text{Na}^+, \text{Rb}^+, \text{Cs}^+$  and  $\text{R} = \text{Y}^{3+}, \text{Yb}^{3+}, \text{Nd}^{3+}$ , etc.) are multifunctional, disordered materials, used as active solid-state luminescent hosts, and their properties could be tailored by different compositions. Among rare earths, neodymium-doped tungstates are widely used for lasing applications owing to their high absorption and emission cross sections.<sup>1</sup> Recently these materials have also been investigated for visible and ultraviolet upconversion from its near-infrared (NIR) origin.<sup>2,3</sup> Crystallographic structures of these materials are related to that of tetragonal Scheelite  $\text{CaWO}_4$ , where  $\text{Ca}^{2+}$  is substituted by an  $\text{A}^+\text{R}^{3+}$  pair.<sup>4</sup> Moreover, distribution of  $\text{R}^{3+}$  ions in host materials leads to distortion in the structure, lowering of symmetry of the parent compound, local environmental disorder, and phase transformations, which eventually results in interesting physical properties as a function of crystal structure.

Interestingly, most of the potassium, rubidium, and cesium rare earth tungstates undergo high temperature polymorphic phase transitions.<sup>5</sup> Klevstova et al.<sup>6</sup> have compiled a detailed review on polymorphism in rare earth double molybdates and tungstates which exhibit a wide range of crystal structures. This structural diversity in the polymorphs results in a difference in

luminescence properties which could be exploited in different optical devices without substantial fluorescence quenching.<sup>7</sup> Recently, Zaldo et al.<sup>5</sup> studied polymorphs of  $\text{AgNdW}_2\text{O}_8$  in detail and correlated their crystal structure with optical bandwidths. On the basis of crystal field analysis, they concluded that the presence of two  $\text{Nd}^{3+}$  sites contributed to the experimental bandwidths.

$\text{KNdW}_2\text{O}_8$  has also been reported to exist in two polymorphic phases:<sup>6</sup> a high temperature tetragonal phase ( $\alpha$ - $\text{KNdW}_2\text{O}_8$ ), which exists above 1000 °C, and a monoclinic phase ( $\beta$ - $\text{KNdW}_2\text{O}_8$ ) at 770 °C. While the crystal structure of the  $\beta$ - $\text{KNdW}_2\text{O}_8$  phase has been elucidated, there have been no crystal structure reports for the  $\alpha$ - $\text{KNdW}_2\text{O}_8$  phase. Kolesov et al.<sup>8</sup> have carried out a Raman study on the monoclinic phase of  $\text{KNdW}_2\text{O}_8$  to illustrate the size and charge effect of  $\text{K}^+$  and  $\text{Nd}^{3+}$  ions on the ordered distribution of cations. Kato et al.<sup>9</sup> has compared the charge compensation effect on photoluminescence spectra of  $\text{KNdW}_2\text{O}_8$  with other smaller alkali rare earth tungstates.  $\text{KNdW}_2\text{O}_8$  exhibits efficient photoluminescence with narrow emission spectra in the IR region which is close to that of  $\text{Nd:YAG}$  at room temperature. Recently, Quereshi et al.<sup>10</sup> demonstrated strong visible light

Received: November 15, 2013

Revised: December 24, 2013

emission from Nd-doped oxide systems. However, little attention has been paid for utilizing neodymium-based tungstates for visible light applications.

In the present study, nanoparticles of  $\alpha$ -KNdW<sub>2</sub>O<sub>8</sub> and micrometer-sized particles of  $\beta$ -KNdW<sub>2</sub>O<sub>8</sub> were synthesized by a solution combustion route. Most of the tungstates are usually synthesized by a ceramic method<sup>11–14</sup> which consumes more energy and time. The solution combustion method is one of the most popular methods as it requires lower temperature and less time to yield smaller-sized particles.<sup>15</sup> The reaction is carried out in the liquid phase thereby achieving more homogeneity and control over the particle size.<sup>16</sup> Moreover, the solution combustion technique is more advantageous in synthesizing both polymorphs by varying fuel amount.

Though many tungstate phosphors have been synthesized by the solution combustion method,<sup>17,18</sup> to our knowledge this is the first report of the synthesis of both polymorphs of KNdW<sub>2</sub>O<sub>8</sub> by this technique. We have carried out detailed crystal structure analysis of the polymorphs using Rietveld quality data obtained from neutron powder diffraction (NPD), which gives the information about average structure with long-range order. It is well-known that photoluminescence behavior is controlled by the local symmetry of the luminescing ion.<sup>19</sup> Deviation from average structure has been observed in many phosphors,<sup>19</sup> and hence analyzing local structure would help in the precise design of new photoluminescent materials. However, to probe any deviation or distortion in the local structure, pair distribution function (PDF) analysis is a more advanced and powerful technique. This real space technique has traditionally been applied to study amorphous materials. PDF measurements involve collecting both the Bragg intensity and diffuse scattering over a wide range of momentum transfer. The PDF thus obtained from the Fourier Transform of the total scattering pattern contains structural information about the local short-, medium-, and long-range order in the material. Since PDF is sensitive to length scales, for the past decade it has been successfully applied to study disorder in crystalline materials, to analyze short-range order, and to complement the average structure analysis. There are many reports in the literature of the unique insights obtained in many materials<sup>20</sup> from probing the local structure at the atomistic level. More details about this method can be found in the literature.<sup>21</sup> Therefore, PDF data obtained from Spallation Neutron Source (SNS) has been utilized in order to explore further the impact of local structure of both polymorphs on photoluminescence behavior. In addition, Raman study of polymorphs establishes the local environment of tungstate ion for both tetragonal and monoclinic phases. Analysis of long-range and short-range order of KNdW<sub>2</sub>O<sub>8</sub> polymorphs from NPD, neutron PDF, and Raman study describes the structural features precisely without any ambiguity.

Although the existence of tetragonal polymorph has been reported earlier,<sup>5</sup> the space group and precise crystal structure were not known. In the current study, while neutron diffraction measurement establishes the symmetry, space group, and average crystal structure, neutron PDF analysis and Raman investigations elucidate the local structure such as the nature of the neodymium and tungstate polyhedra in both polymorphs.

In summary, the current work aims to correlate the crystal structure of both polymorphs with observed photoluminescence for the first time in the visible region for KNdW<sub>2</sub>O<sub>8</sub>. This study indicates that these polymorphs can be considered as promising phosphors in solid state lighting devices that can

luminesce in the blue, green, and red region depending on the excitation wavelength.

## 2. EXPERIMENTAL SECTION

**2.1. Synthesis.** Both the polymorphs of KNdW<sub>2</sub>O<sub>8</sub> were synthesized by the solution combustion method. In this technique, at a lower ignition temperature, an exothermic reaction between fuel and oxidizer takes place in a remarkably short time at the reaction site. The present synthesis protocol utilizes Nd(NO<sub>3</sub>)<sub>3</sub>·xH<sub>2</sub>O, KNO<sub>3</sub>, and H<sub>40</sub>N<sub>10</sub>W<sub>12</sub>O<sub>41</sub>·H<sub>2</sub>O as precursors and urea as a fuel to synthesize both polymorphs. Thus,  $\alpha$ -KNdW<sub>2</sub>O<sub>8</sub> and  $\beta$ -KNdW<sub>2</sub>O<sub>8</sub> were obtained by varying the fuel amount and reaction temperature.

**2.1.1. Synthesis of  $\alpha$ -KNdW<sub>2</sub>O<sub>8</sub>.** In a typical procedure, an aqueous redox mixture of a stoichiometric amount of Nd(NO<sub>3</sub>)<sub>3</sub>·xH<sub>2</sub>O, KNO<sub>3</sub>, and H<sub>40</sub>N<sub>10</sub>W<sub>12</sub>O<sub>41</sub>·H<sub>2</sub>O with 4 g of urea were taken in a 50 mL silica crucible and introduced into a muffle furnace preheated at 600 °C. The solution boils at high temperatures, ignites, and undergoes a self-sustained reaction to yield violet flaky powder. The obtained sample was annealed at 600 °C for 6 h to obtain a pure phase of  $\alpha$ -KNdW<sub>2</sub>O<sub>8</sub>.

**2.1.2. Synthesis of  $\beta$ -KNdW<sub>2</sub>O<sub>8</sub>.** The procedure followed is same as that of section 2.2.1 except that the amount of fuel was reduced to 2 g and the annealing temperature was higher. Fuel and redox mixture were placed in a muffle furnace preheated at 600 °C and maintained at the same temperature for 2 h. Then, the temperature was increased rapidly to 770 °C and kept for 12 h. Violet powder of  $\beta$ -KNdW<sub>2</sub>O<sub>8</sub> was obtained.

**2.2. Characterization.** **2.2.1. X-ray Diffraction (XRD).** Phase purity of both polymorphs was confirmed by Bruker, D2 phaser X-ray powder diffractometer with Cu K $\alpha$  (1.5418 Å) radiation (Figure 1, Supporting Information).

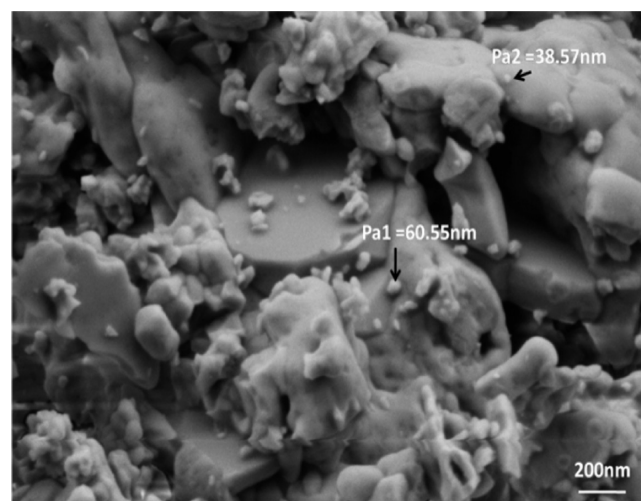


**Figure 1.** SEM photograph of  $\alpha$ -KNdW<sub>2</sub>O<sub>8</sub>; scale shows 200 nm.

**2.2.2. Neutron Diffraction Data Collection.** Time-of-flight powder neutron diffraction data were collected at Nanoscale-Ordered Materials Diffractometer (NOMAD) at SNS, Oak Ridge National Laboratory. Data were collected for ~200 mg of both polymorphs in a sealed vanadium can. Data were collected at room temperature for 2 h. After normalization of observed intensities by scattering from a vanadium rod and subtracting of the background scattering from the empty container, the experimental PDF was obtained by a Fourier transform of the total scattering structure function  $S(Q)$  up to  $Q_{\max}$  of 35 Å<sup>-1</sup>. Instrument resolution parameters,  $Q_{\text{damp}} = 0.017$  Å<sup>-1</sup> and  $Q_{\text{broad}} = 0.036$  Å<sup>-1</sup>, were determined with Ni bulk powder (99.99%, Sigma Aldrich) measured under similar conditions. The program PDFgui<sup>23</sup> was used to perform fits in real space on the observed data to obtain local structural information.

**2.2.3. Raman Study.** Raman spectra was recorded in the 180° backscattering geometry, using a 532 nm excitation from a diode



pumped frequency doubled Nd:YAG solid state laser (model GDL-5015 L, Photop Suwtech Inc., China) and a custom-built Raman spectrometer equipped with a SPEX TRIAX 550 monochromator and a liquid nitrogen cooled CCD (Spectrum One with CCD 3000 controller, ISA Jobin Yvon). Laser power at the sample was  $\approx 8\text{ mW}$ , and a typical spectral acquisition time was 1 min. The spectral resolution chosen was  $2\text{ cm}^{-1}$ , and the spectral profile was fitted using Lorentzian functions with the appropriate background.

**2.2.4. SEM Analysis and Optical Measurements.** The morphology and particle size of both polymorphs were investigated by Ultra 55 Carl Zeiss FE-SEM.

Excitation and emission spectra were recorded by a Perkin-Elmer photoluminescence spectrophotometer at room temperature with Xe lamp as a source.

### 3. RESULTS AND DISCUSSION

**3.1. Synthesis.** Klevstov et al.<sup>6</sup> in their comprehensive review mentioned the formation of high temperature phase of  $\text{KNdW}_2\text{O}_8$  ( $\alpha\text{-KNdW}_2\text{O}_8$ ) to have a  $\text{CaWO}_4$  structure type and reported the monoclinic phase as low temperature modification ( $\beta\text{-KNdW}_2\text{O}_8$ ). Bulk  $\alpha\text{-KNdW}_2\text{O}_8$  prepared at  $1020^\circ\text{C}$  by the ceramic method was found to be isostructural to tetragonal  $\text{AgNdW}_2\text{O}_8$ .<sup>5</sup> The  $\beta\text{-KNdW}_2\text{O}_8$  phase was synthesized at  $770^\circ\text{C}$  for 48 h, and the X-ray pattern matched ICSD card number 9364. In the current work,  $\alpha\text{-KNdW}_2\text{O}_8$  and  $\beta\text{-KNdW}_2\text{O}_8$  have been achieved from the solution combustion method. Controlling the fuel to oxidizer ratio is crucial to obtain the desired phase. Specifically, a higher fuel to oxidizer ratio raises the temperature of the system to a large extent, leading to formation of  $\alpha\text{-KNdW}_2\text{O}_8$ . Alternatively, as the fuel amount decreases, heat evolved in the reaction system decreases favoring formation of  $\beta\text{-KNdW}_2\text{O}_8$ . Contrary to the ceramic method, the larger fuel to oxidizer ratio favors the formation of  $\alpha\text{-KNdW}_2\text{O}_8$  at lower synthesis temperature. Since the fuel amount is directly proportional to the temperature of the reaction system, it is possible to synthesize both phases of  $\text{KNdW}_2\text{O}_8$  by this technique. Thus, the solution combustion technique is preferred over the solid state technique as it is more efficient and needs less time.

**3.2. SEM Analysis.** To get detailed information of morphology of the products, SEM analysis was performed. Figures 1, 2, and 3 illustrate SEM images of  $\alpha\text{-KNdW}_2\text{O}_8$  and  $\beta\text{-KNdW}_2\text{O}_8$ . Combustion synthesis resulted in mixed morphology and smaller particles for  $\alpha\text{-KNdW}_2\text{O}_8$ . The

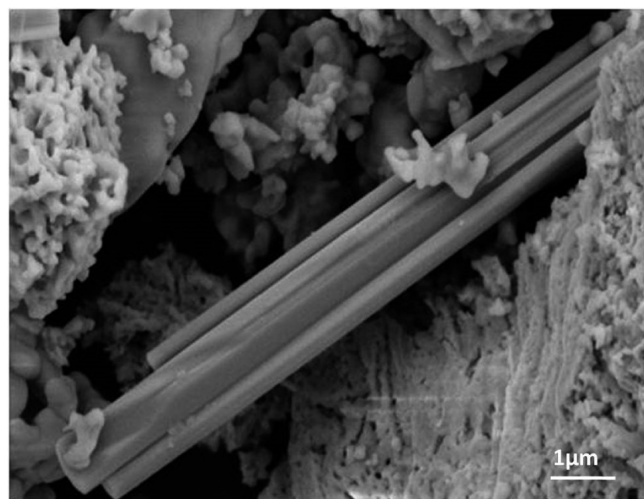


Figure 2. SEM photograph of  $\alpha\text{-KNdW}_2\text{O}_8$ ; scale shows  $1\text{ }\mu\text{m}$ .

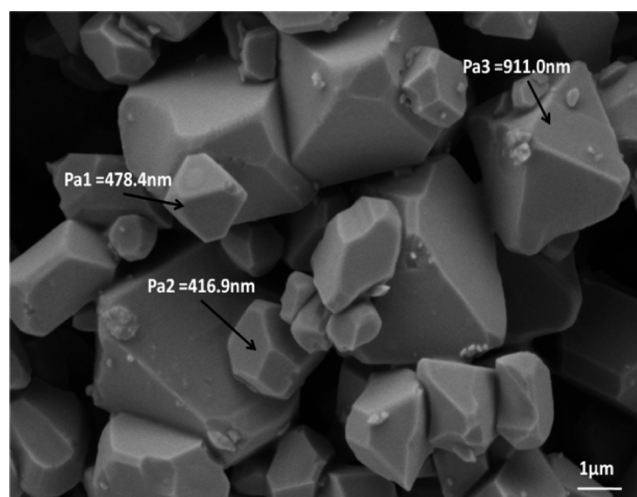
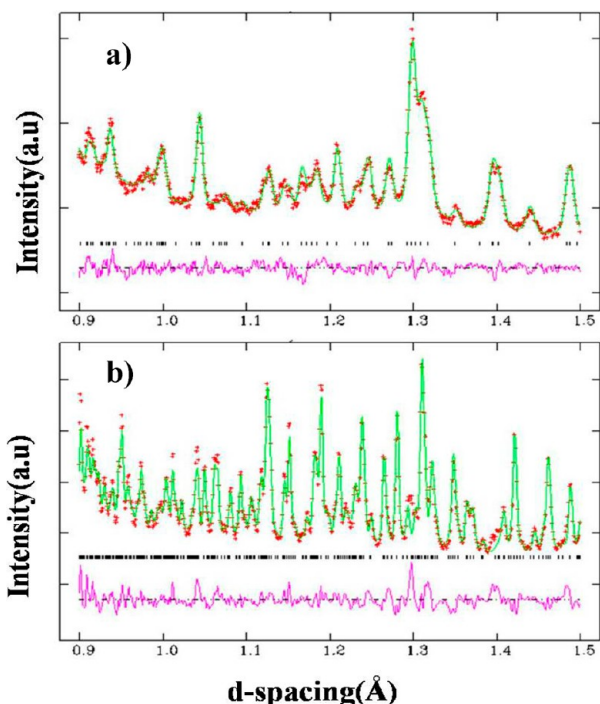


Figure 3. SEM photograph of  $\beta\text{-KNdW}_2\text{O}_8$ .

majority of particles (Figures 1 and 2) have spherical and platelike morphology with a few rodlike particles scattered between. Spherical shaped particles are in the  $30\text{--}70\text{ nm}$  range; platelike shaped particles are bigger, while rodlike shaped particles fall in the micrometer regime. Usually in combustion synthesis, final morphology of crystal deviates from equilibrium crystal shape (ECS) due to external factors such as (a) pH of reaction mixture, (b) annealing temperature, and (c) mass of the reactants.<sup>24</sup> Formation of rodlike particles could be correlated with the high temperature and heating rate of combustion synthesis.<sup>25</sup> Su Qingde et al.<sup>26</sup> have shown that during combustion reaction in some areas such as tip of the flame, very high temperatures result in aggregation of some particles. We surmise that this phenomenon could be responsible for the anisotropic aggregation of few particles in  $\alpha\text{-KNdW}_2\text{O}_8$  resulting in rodlike shapes. The SEM image of  $\beta\text{-KNdW}_2\text{O}_8$  (Figure 3) shows a larger but homogeneous distribution of pyramidal shaped particles, ranging from  $415\text{ nm}$  to about  $1\text{ }\mu\text{m}$  in size. The larger particle size could be attributed to a higher calcination temperature. The particle shape can be explained on the basis of ECS, driven by reduction of surface energy.<sup>27</sup> Spherical-shaped particles tend to attain lower surface energy faceted crystals. In the case of  $\beta\text{-KNdW}_2\text{O}_8$ , this faceting process might be incomplete, resulting in formation of intermediate pyramidal-shaped particles.

**3.3. Neutron Powder Diffraction (NPD).** **3.3.1. Profile Refinement of  $\alpha\text{-KNdW}_2\text{O}_8$ .** Rietveld refinement of NPD was performed in order to determine the position of oxygens accurately. The model proposed by Colon et al.<sup>5</sup> in space group  $I\bar{4}$  was taken as the initial model and structures were refined to completion using the GSAS/EXPGUI package.<sup>28</sup> Profile was fitted by using a pseudo-Voigt function, and a shifted Chebyshev function consisting of  $10\text{--}15$  parameters was applied to define the background. Since all heavy atoms were in a special position, only oxygen positional parameters were refined to convergence while the thermal parameter and occupancy were held fixed. Then occupancies of Nd and K atoms in the same site were refined, while the overall occupancy of the crystallographic site was held fixed. Isotropic thermal parameters of Nd and K atoms were then refined alternately with occupancies. The thermal parameters of tungsten and oxygen atoms were constrained and refined.

**3.3.2. Profile Refinement of  $\beta$ -KNdW<sub>2</sub>O<sub>8</sub>.** XRD confirms the formation of monoclinic phase of  $\beta$ -KNdW<sub>2</sub>O<sub>8</sub> (ICSD card number 9364). Hence, Rietveld refinement of NPD data was carried out in  $C2/m$  space group using GSAS suite.<sup>28</sup> A pseudo-Voigt function was used to fit the profile. A shifted Chebyshev function consisting of 25 parameters was applied to define the background. The same refinement strategy followed for  $\alpha$ -KNdW<sub>2</sub>O<sub>8</sub> was employed. Since potassium and neodymium atoms occupy two different lattice sites, occupancy was refined separately. Calculated, observed, and difference patterns of both polymorphs are shown in Figure 4. Occupancy, thermal parameters, and positions of all the atoms are listed in the Table 1. Details of crystallographic data of both polymorphs are in Table 2.



**Figure 4.** Observed, calculated, and difference neutron powder diffraction profiles for (a)  $\alpha$ -KNdW<sub>2</sub>O<sub>8</sub> and (b)  $\beta$ -KNdW<sub>2</sub>O<sub>8</sub>.

**3.3.3. Crystal Structure of Tetragonal  $\alpha$ -KNdW<sub>2</sub>O<sub>8</sub> and Monoclinic  $\beta$ -KNdW<sub>2</sub>O<sub>8</sub>.** Figure 5a depicts a structural view of  $\alpha$ -KNdW<sub>2</sub>O<sub>8</sub> along the '*a*' direction. In the crystal structure, K and Nd atoms occupy the special position with 4 symmetry. Occupancy refinements carried out on tetragonal  $\alpha$ -KNdW<sub>2</sub>O<sub>8</sub> confirm that K and Nd atoms occupy the same crystallographic sites (2b and 2d Wyckoff positions) and are statistically distributed. Further, the structural analysis shows  $\alpha$ -KNdW<sub>2</sub>O<sub>8</sub> has two types of K and Nd atoms which are coordinated to eight oxygen atoms forming two different regular Nd/K–O<sub>8</sub> polyhedra with two different bond distances (Table 3). There are two different types of tungsten tetrahedra, that is, W1O<sub>4</sub> and W2O<sub>4</sub>, which are regular and do not show any distortion. All the heavy elements are isolated; that is, no two potassium/neodymium or tungstens are connected directly.

The crystal structure of  $\beta$ -KNdW<sub>2</sub>O<sub>8</sub> along the '*c*' direction is illustrated in Figure 5b.  $\beta$ -KNdW<sub>2</sub>O<sub>8</sub> refines in centrosymmetric monoclinic  $C2/m$  space group. The volume of the unit cell is almost double that of  $\alpha$ -KNdW<sub>2</sub>O<sub>8</sub>, due to loss of 4-fold symmetry. All the cations are connected through oxygen ions

forming a cage-like structure. Neodymium and potassium atom occupy 4i and 4g positions, respectively, in asymmetric unit and are surrounded by eight oxygen ions. There are two crystallographically different tungsten atoms in 4h and 4i sites which are associated to 2-fold and mirror symmetry, respectively, resulting in two different tungsten octahedra in the crystal structure. The octahedra are edge sharing in every unit cell with W1O<sub>6</sub> octahedra sharing three edges and W2O<sub>6</sub> octahedra sharing only two edges as shown in Figure 6a. The tungsten ions form a W<sub>2</sub>O<sub>2</sub> bridge resulting in a W<sub>4</sub>O<sub>16</sub> unit as shown in Figure 6b. Table 3 lists selected bond distances and co-ordination number of both phases obtained from the Rietveld refinements. It is apparent from the W–O bond distances listed in Table 3 (NPD) that tungsten octahedra are distorted, and distances are longer than  $\alpha$ -KNdW<sub>2</sub>O<sub>8</sub>. In the case of Nd–O polyhedra, a wider distribution of bond lengths resulting in distorted NdO<sub>8</sub> polyhedra is observed (Table 3). The short and long W–O bond distances of distorted tungsten octahedra could result in the difference in bond lengths of NdO<sub>8</sub> polyhedra in monoclinic phase.

### 3.4. Local Structure of Tetragonal $\alpha$ -KNdW<sub>2</sub>O<sub>8</sub> and Monoclinic $\beta$ -KNdW<sub>2</sub>O<sub>8</sub>.

**3.4.1. PDF Measurements.** The sensitivity of the PDF to short-range structure and local bond distance is advantageous to probe changes in the orientation and geometry of the polyhedra in crystalline materials, especially over low *r* ranges. Thus, PDF analysis was carried out to obtain local structure information of variations in bond lengths in tungsten and the luminescent Nd polyhedra. This, we believe, is essential to understand the influence of structural changes to the observed optical properties.

The structural parameters obtained from Rietveld refinement were adopted as an initial model for local structure analysis for both  $\alpha$ -KNdW<sub>2</sub>O<sub>8</sub> and  $\beta$ -KNdW<sub>2</sub>O<sub>8</sub> using the program PDFgui. Since PDF is a function in real-space, the range over which refinement is carried out can be varied from average to local atom–atom distances. Therefore, refinements were carried out in the lower *r* range from 1.5 Å to 3.0 Å. Figure 7 shows well-fitted PDF for both polymorphs. Details of crystallographic parameters obtained from PDF refinements are listed in Table 2. Table 3 compares the bond lengths obtained from low *r* PDF refinements and the Rietveld method. The W–O bond distribution observed for  $\alpha$ -KNdW<sub>2</sub>O<sub>8</sub> around 1.77 Å–1.88 Å confirms the presence of two regular W–O polyhedra in  $\alpha$ -KNdW<sub>2</sub>O<sub>8</sub>. The narrower peak width and higher intensity of the first W–O peak of  $\alpha$ -KNdW<sub>2</sub>O<sub>8</sub> substantiate this, since it is well-known that intensity of a PDF peak located at *r* is proportional to the number of atom pairs separated by distance *r*. PDF refinements also show the bond distribution and coordination of the K/Nd ion which is in good agreement with the results obtained from Rietveld refinements. The only minor difference is that K1/Nd1–O1 bond is longer, while the K2/Nd2–O1 bond is shorter at the low *r* range. Furthermore, Nd–O bond lengths are regular and show no distortion (Figure 8a).

Analysis of PDF in the *r* range 1.5–3.0 Å for  $\beta$ -KNdW<sub>2</sub>O<sub>8</sub> is shown in Figure 7b. Examination of bond lengths of  $\beta$ -KNdW<sub>2</sub>O<sub>8</sub> (Table 3) shows a variable bond length distribution for W1–O and W2–O distances, emphasizing the distortion in W–O polyhedra. This observation has been amply substantiated by Rietveld refinement data. Since all cations are connected by oxygen atoms, the distortion in WO<sub>6</sub> octahedra could consequently result in short and long Nd–O bond lengths varying in the range from 2.36 Å (short) to 2.52 Å (long) present. Thus, it could be concluded that NdO<sub>8</sub>

Table 1. Atomic Coordinates, Isotropic Thermal Parameters, and Occupancy Obtained from Rietveld Refinement

atom	site	x	y	z	U (Å <sup>2</sup> )	occupancy
(a) $\alpha$ -KNdW <sub>2</sub> O <sub>8</sub>						
K(1)	2d	0.500	0.000	0.250	0.002(3)	0.34(1)
Nd(1)	2d	0.500	0.000	0.250	0.002(3)	0.66(1)
K(2)	2b	0.500	0.500	0.000	0.012(2)	0.66(1)
Nd(2)	2b	0.500	0.500	0.000	0.012(2)	0.34(1)
W(1)	2a	0.000	0.000	0.000	0.010(1)	1.00
W(2)	2c	0.000	0.500	0.250	0.010(1)	1.00
O(1)	8g	0.222(1)	−0.128(1)	0.082(1)	0.017(1)	1.00
O(2)	8g	0.248(1)	−0.651(1)	0.173(1)	0.017 (1)	1.00
(b) $\beta$ -KNdW <sub>2</sub> O <sub>8</sub>						
K(1)	4i	0.187(1)	0.500	0.519(1)	0.013(1)	1.00
Nd(1)	4g	0.000	0.303(1)	0.000	0.003(2)	1.00
W(1)	4h	0.500	0.341(1)	0.500	0.006(1)	1.00
W(2)	4i	0.301(1)	0.500	0.059(1)	0.006(1)	1.00
O(1)	8j	0.282 (1)	0.373(1)	0.331(1)	0.022(3)	1.00
O(2)	8j	0.043(1)	0.264(1)	0.271(1)	0.004(3)	1.00
O(3)	4i	0.423(1)	0.000	0.100(1)	0.033(3)	1.00
O(4)	8j	0.168(1)	0.128(1)	0.067(1)	0.022(3)	1.00
O(5)	4i	0.017(1)	0.000	0.342(1)	0.032(3)	1.00

Table 2. Crystallographic Data of  $\alpha$ -KNdW<sub>2</sub>O<sub>8</sub> and of  $\beta$ -KNdW<sub>2</sub>O<sub>8</sub> Obtained from Rietveld Analysis and PDF

	(a) $\alpha$ -KNdW <sub>2</sub> O <sub>8</sub>		(b) $\beta$ -KNdW <sub>2</sub> O <sub>8</sub>	
	NPD	PDF	NPD	PDF
space group	$\bar{1}4$	$\bar{1}4$	$C2/m$	$C2/m$
a (Å)	5.404(2)	5.390(2)	10.173(2)	10.180(2)
b (Å)	5.404(2)	5.390(2)	10.772(1)	10.690(1)
c (Å)	11.980(6)	12.020(6)	7.495(1)	7.500(1)
$\alpha$ (degree)	90	90	90	90
$\beta$ (degree)	90	90	126.10(1)	126.01(1)
$\gamma$ (degree)	90	90	90	90
volume of unit cell (Å <sup>3</sup> )	349.77(3)	349.21(3)	664.30(3)	658.49(3)
$R_{wp}$ (%)	3.63	19.53	10.15	19.01
$R_p$	3.33		7.49	
$R(I, hkl)$ (%)	8.67		9.20	

polyhedra in  $\beta$ -KNdW<sub>2</sub>O<sub>8</sub> is distorted compared to  $\alpha$ -KNdW<sub>2</sub>O<sub>8</sub> (Figure 8b). It is also observed that K–O bond distances are slightly different than that obtained from Rietveld analysis.

From the above detailed studies, two complementary techniques, neutron Rietveld and PDF analysis, reveal the distortions in K/Nd–O polyhedra and also confirm the change of W–O polyhedra from tetrahedral geometry in  $\alpha$ -KNdW<sub>2</sub>O<sub>8</sub> to octahedral coordination in  $\beta$ -KNdW<sub>2</sub>O<sub>8</sub>. Luminescence is largely determined by the geometry around luminescent centers, that is, in this case Nd ions. Previously, it has been reported that the intermolecular interactions through bridging anionic tungstate layer of KYb(WO<sub>4</sub>)<sub>2</sub><sup>29</sup> result in a marked broadening of its emission and absorption bands. In  $\beta$ -KNdW<sub>2</sub>O<sub>8</sub> phase, the presence of W–O bridging bonds with edge-shared tungstate octahedra therefore could also influence the photoluminescence behavior by distorting the luminescing polyhedra.<sup>30</sup> Hence, we believe that the distortion in the WO<sub>6</sub> octahedra could indirectly contribute to intensity and bandwidth of photoluminescence in the  $\beta$ -KNdW<sub>2</sub>O<sub>8</sub> phase. Thus, we have attempted to study the intermolecular interactions in the tungstate octahedral using Raman spectroscopy.

**3.4.2. Raman Study.** The normal-mode analysis of a free tetrahedral WO<sub>4</sub><sup>−2</sup> ion predicts its fundamental vibrational frequencies at  $\nu_1$  (A<sub>1</sub>):928,  $\nu_2$  (E):320,  $\nu_3$  (F<sub>2</sub>):833, and  $\nu_4$

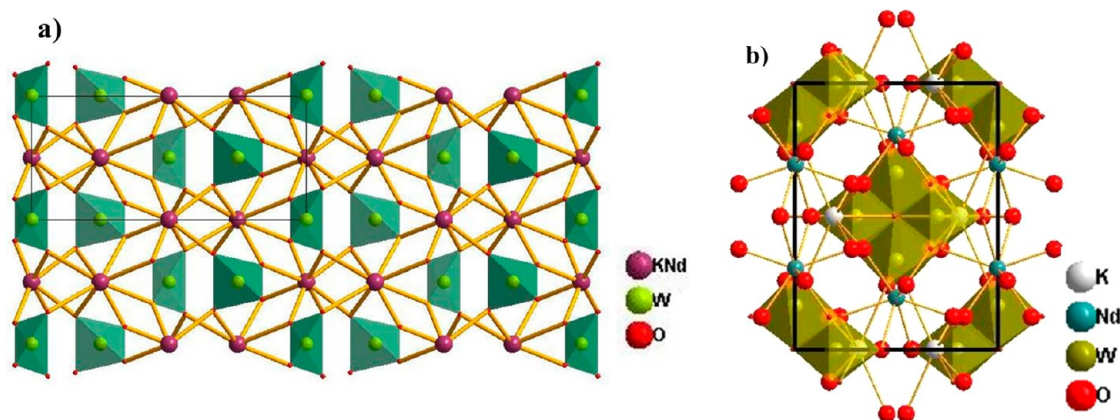
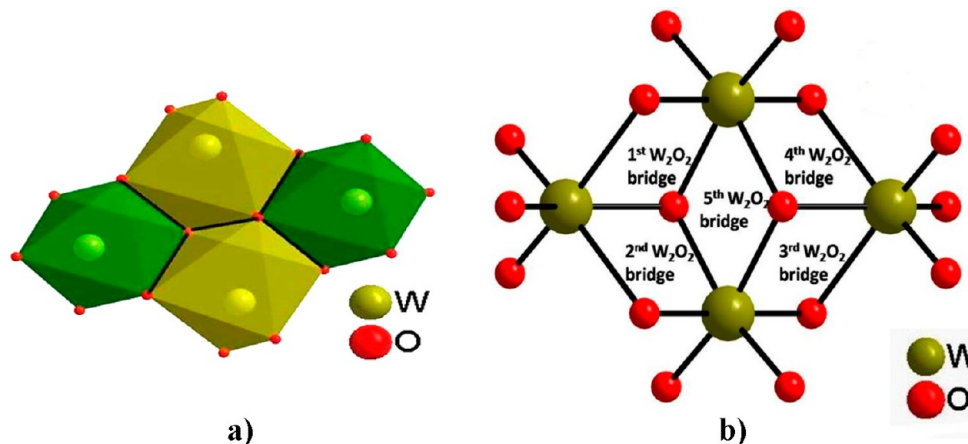
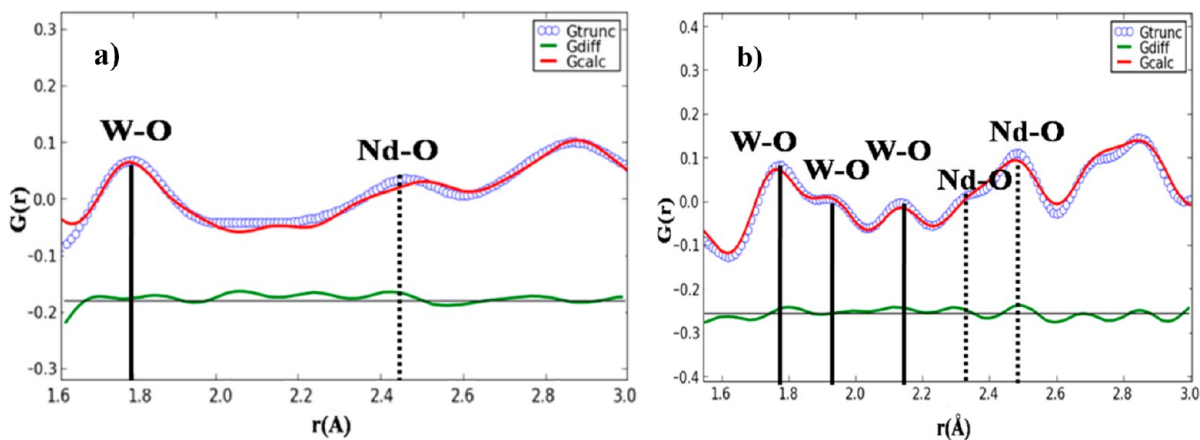
Figure 5. Structural representation of (a)  $\alpha$ -KNdW<sub>2</sub>O<sub>8</sub> along the *a* direction and (b)  $\beta$ -KNdW<sub>2</sub>O<sub>8</sub> along the *c* direction.



Table 3. Selected Bond Distances of  $\alpha$ -KNdW<sub>2</sub>O<sub>8</sub> and  $\beta$ -KNdW<sub>2</sub>O<sub>8</sub>

bond length (Å)				bond length (Å)			
bond type	CN	NPD	PDF	bond type	CN	NPD	PDF
(a) Selected Bond Distance of $\alpha$ -KNdW <sub>2</sub> O <sub>8</sub>							
K1/Nd1—O1	4	2.60(1)	2.82(1)	W1—O1	4	1.70(1)	1.70(1)
K1/Nd1—O2	4	2.50(1)	2.49(1)	W1—O2	4	1.81(2)	1.87(1)
K2/Nd2—O1	4	2.69(1)	2.47(1)				
K2/Nd2—O2	4	2.61(1)	2.60(1)				
(b) Selected Bond Distance of $\beta$ -KNdW <sub>2</sub> O <sub>8</sub>							
K1—O1	2	2.96(1)	2.98(1)	W1—O1	2	1.89(1)	1.84(1)
K1—O2	2	2.83(1)	2.68(1)	W1—O2	2	1.82(1)	1.90(1)
K1—O3	2	2.68(1)	2.64(1)	W1—O5	2	2.14(1)	2.07(1)
K1—O4	1	2.92(1)	2.80(1)				
K1—O5	1	2.53(1)	2.66(1)	W2—O1	2	2.13(1)	2.12(1)
Nd1—O1	2	2.45(1)	2.52(1)	W2—O3	1	1.85(1)	1.85(1)
Nd1—O2	2	2.43(1)	2.36(1)	W2—O4	2	1.85 (1)	1.85 (1)
Nd1—O3	1	2.53(1)	2.48(1)	W2—O5	1	1.97(1)	2.07 (1)
Nd1—O4	2	2.40(1)	2.39(1)				

Figure 6. Structural view depicting (a) edge-sharing tungstate octahedron in  $C2/m$  and (b)  $W_4O_{16}$  unit formed by the  $W_2O_2$  bridge interaction in  $\beta$ -KNdW<sub>2</sub>O<sub>8</sub>.Figure 7. Observed (blue), calculated (red), and difference (green) pattern PDFs for (a)  $\alpha$ -KNdW<sub>2</sub>O<sub>8</sub> and (b)  $\beta$ -KNdW<sub>2</sub>O<sub>8</sub> for  $Q_{\max} = 35 \text{ \AA}^{-1}$ .

( $F_2$ ):405  $\text{cm}^{-1}$ , where  $\nu_1$ : the symmetric stretching mode,  $\nu_2$ : the doubly degenerate symmetric bending mode,  $\nu_3$ : the triply degenerate asymmetric stretching mode, and  $\nu_4$ : the triply degenerate asymmetric bending mode. However, when the symmetry of  $WO_4^{2-}$  in the crystalline environment lowers, band positions will shift and also split.

Generally, in the solid state, isolated tetrahedra show stretching modes in the range 750–1000  $\text{cm}^{-1}$  and bending modes in the range 250–430  $\text{cm}^{-1}$  (Table 1, Supporting Information), whereas the translational and librational modes appear below 250  $\text{cm}^{-1}$ . The compound in the present study exhibits two polymorphic structures, one in tetragonal phase with space group  $I\bar{4}$  and the other in the monoclinic phase with

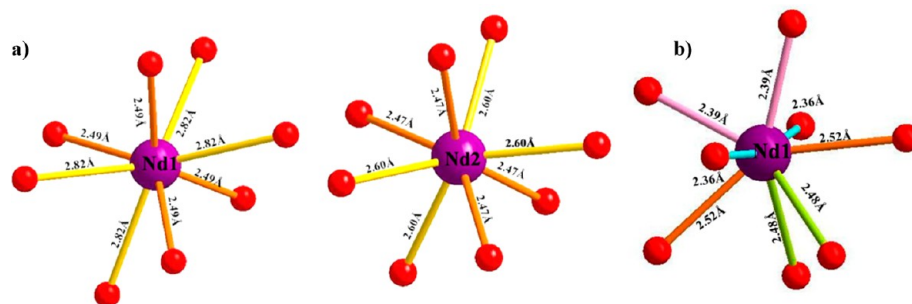


Figure 8.  $\text{NdO}_8$  polyhedron in (a)  $I\bar{4}$  and (b)  $C2/m$ .

space group  $C2/m$  as explained above (Table 2). In the tetragonal phase, the structure contains two independent  $\text{WO}_4$  units in the asymmetric unit, and both  $\text{WO}_4$  units remain isolated from each other (Figure 9). However, in the

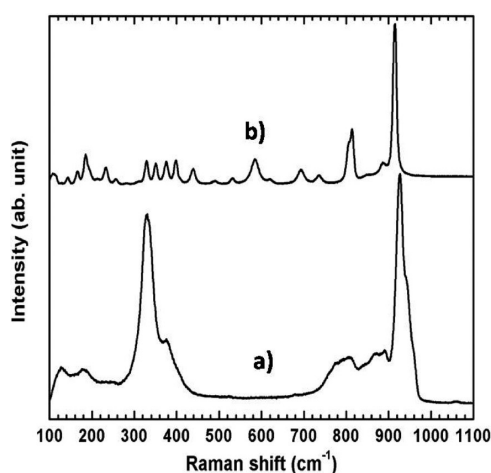


Figure 9. Raman spectra of (a)  $\alpha\text{-KNdW}_2\text{O}_8$  and (b)  $\beta\text{-KNdW}_2\text{O}_8$  in the frequency range 100–1100  $\text{cm}^{-1}$ .

monoclinic phase W atoms are coordinated with six oxygen atoms forming  $\text{WO}_6$  octahedra which are connected to each other via a  $\text{W}_2\text{O}_2$  bridge resulting in a  $\text{W}_4\text{O}_{16}$  unit (Figure 6b). Figure 10 represents Raman spectra of the two polymorphs collected in the frequency range 120–1100  $\text{cm}^{-1}$  and at 298 K. All the Raman active modes of both polymorphs are assigned based on information available in the literature.<sup>31</sup> Raman spectrum of the  $\beta\text{-KNdW}_2\text{O}_8$  structure has more Raman active frequencies compared to the  $\alpha\text{-KNdW}_2\text{O}_8$  structure. The appearance of new Raman active bands is a definite indication that the coordination number of W is more than four as it should be due to the presence of oxygen bridge vibrations.<sup>29</sup> This is supported by NPD results, where the coordination number of W is observed to increase from four to six (Figure 6a and Table 3). The vibrational frequencies present in monoclinic polymorph indicate a particular type of  $\text{W}_2\text{O}_2$  bridge interactions which was explained elsewhere.<sup>32</sup> For the  $\alpha\text{-KNdW}_2\text{O}_8$  structure, the symmetric W–O stretching region ( $\nu_1$ ) has an intense and well-defined Raman peak centered at 955 and two shoulders at 940 and 925  $\text{cm}^{-1}$ . The asymmetric W–O stretching region ( $\nu_3$ ) appears with large splitting and contains six Raman active frequencies centered at 892, 867, 840, 810, 790, 776  $\text{cm}^{-1}$ . The asymmetric ( $\nu_4$ ) and symmetric ( $\nu_2$ ) bending frequencies appear at 400, 377, and 329  $\text{cm}^{-1}$ , while the  $\text{K}^+$  and  $\text{Nd}^{3+}$  translational modes appear at 245 and

179  $\text{cm}^{-1}$ . For  $\beta\text{-KNdW}_2\text{O}_8$ , the symmetric W–O stretching frequency ( $\nu_1$ ) appears as a strong peak at 915  $\text{cm}^{-1}$ , whereas the asymmetric W–O stretching frequencies ( $\nu_3$ ) appear at 886, 848, 813, and 806  $\text{cm}^{-1}$ . The  $\text{W}_2\text{O}_2$  bridge stretching frequencies appear at 736, 693  $\text{cm}^{-1}$  and the W–O–W stretching modes are at 619, 585, 532, 490, 439, 398  $\text{cm}^{-1}$ . The O–W–O and W–O–W bending regions frequencies are centered at 375, 350, 329 and 308, 281  $\text{cm}^{-1}$ . However, the  $\text{K}^+$ ,  $\text{Nd}^{3+}$ , and  $\text{WO}_6$  translational modes appear at 256, 232; 214, 194, 185, 166, 143, 128  $\text{cm}^{-1}$ . The combined neutron diffraction and Raman measurements clearly confirm the change in coordination of tungsten polyhedra. The  $\text{W}_2\text{O}_2$  bridge determined from neutron diffraction analysis is verified from Raman analysis (Figure 6b). The distortion in the  $\text{WO}_6$  octahedra could be responsible for the variable bond lengths and distortion of Nd polyhedra.

Thus, two effects, that is, the occupational disorder and the degree of distortion of the Nd polyhedra, need to be considered in the discussion of the photoluminescence behavior (section 3.5). In the tetragonal system ( $I\bar{4}$ ), the Nd ions share two nonequivalent crystallographic sites (2b and 2d Wyckoff positions) with the K ions resulting in an intrinsic occupational disorder, while in the monoclinic phase ( $C2/m$ ), the  $\text{Nd}^{3+}$  ion occupy a crystallographically distinct site. Zaldo et al.<sup>5</sup> reports that disordered ( $I\bar{4}$ ) and ordered ( $C2/m$ ) systems contribute to the difference in the bandwidth of the photoluminescent lines. Additionally, the environment around the luminescing ion, that is, the coordination of Nd ion could also affect the luminescent properties.

**3.5. Photoluminescent Behavior.** Figure 10 represents the excitation spectra examined at 597 nm for  $^4\text{G}_{5/2} \rightarrow ^4\text{I}_{9/2}$  emission of Nd ion for both polymorphs.<sup>33</sup> The excitation peaks can be attributed to the electrical transition of  $\text{Nd}^{3+}$  ion present in the host matrix. The excitation band at 355 nm is responsible for the transition from  $^4\text{I}_{9/2} \rightarrow ^4\text{D}_{5/2}$ , 399 nm for  $^4\text{I}_{9/2} \rightarrow ^2\text{P}_{3/2}$ ,<sup>34</sup> for 447 nm  $^4\text{I}_{9/2} \rightarrow ^2\text{P}_{1/2}$  transition.<sup>33</sup> The peak centered at 466 nm and 490 nm corresponds to excitation from  $^4\text{I}_{9/2} \rightarrow ^4\text{G}_{11/2}$ . The peak at 547 nm is related to the  $^4\text{I}_{9/2} \rightarrow ^4\text{G}_{7/2}$  transition of the Nd ion for  $\alpha\text{-KNdW}_2\text{O}_8$ . Similar transitions are observed in the case of  $\beta\text{-KNdW}_2\text{O}_8$  except that all peaks are red-shifted by around 5 nm with respect to  $\alpha\text{-KNdW}_2\text{O}_8$ . Two excitation wavelengths, one in the near UV region, that is, 355 nm, and another one from the green region (545 nm) were chosen to investigate the emission spectra in the visible region. It is evident from the excitation spectra that both polymorphs can be efficiently excited in the UV region (355 nm) as well as in the green region (545 nm). Figure 11 shows the emission spectra of both polymorphs excited at 355 nm.



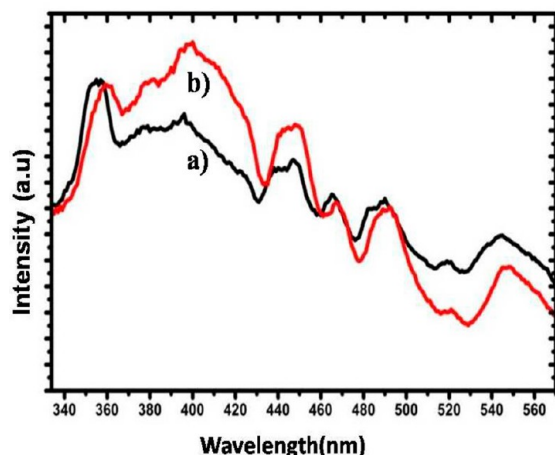


Figure 10. Excitation spectra of (a)  $\alpha$ -KNdW<sub>2</sub>O<sub>8</sub> and (b)  $\beta$ -KNdW<sub>2</sub>O<sub>8</sub> monitored at 597 nm.

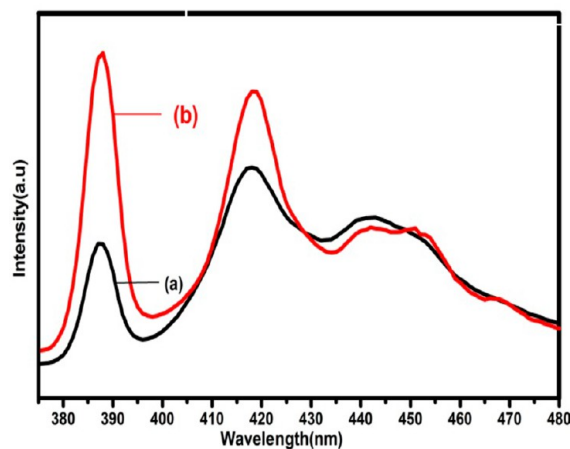


Figure 11. Emission spectra of (a)  $\alpha$ -KNdW<sub>2</sub>O<sub>8</sub> and (b)  $\beta$ -KNdW<sub>2</sub>O<sub>8</sub> excited at 355 nm.

Intracation in 4f levels of Nd<sup>3+</sup> ion is responsible for observed emission peaks. The photoluminescence spectra in Figure 11 consist of two major emission peaks at 388 nm and 419 nm in the near UV region corresponding to the excitations from  $^2P_{3/2} \rightarrow ^4I_{9/2}$  and  $^2D_{5/2} \rightarrow ^4I_{9/2}$ , respectively.<sup>5</sup> The broad peak obtained in the range from 434 nm to 480 nm emission corresponding to blue region could be due to  $^4G_{9/2} + ^2D_{3/2} + ^4G_{11/2} + ^2K_{15/2}$  to  $^4I_{9/2}$  transitions.<sup>5</sup> It is observed that these transitions have different multiplicities, and this could also be attributed to the spin–orbital coupling that is predominantly observed in rare earth ions.<sup>35</sup> A detailed theoretical calculation would be necessary to ascertain the spin and orbital contributions to the transitions. The peak width in  $\alpha$ -KNdW<sub>2</sub>O<sub>8</sub> leads to statistical disorder induced by Nd and K atoms sharing the same crystallographic site. Nevertheless, it is apparent that the peaks in  $\beta$ -KNdW<sub>2</sub>O<sub>8</sub> are broader compared to  $\alpha$ -KNdW<sub>2</sub>O<sub>8</sub>. This could be because the distorted octahedral coordination of the W–O octahedra causes long and short bonds in the NdO<sub>8</sub> polyhedra present in the lower symmetry  $\beta$ -KNdW<sub>2</sub>O<sub>8</sub> producing broader spectral band widths. Previous reports show that emission peaks in the photoluminescence spectra of monoclinic KEuW<sub>2</sub>O<sub>8</sub><sup>36</sup> are broader than the photoluminescence peaks in tetragonal NaEuW<sub>2</sub>O<sub>8</sub>. The authors have explained that the observed broadness is a

consequence of deviation in the metal–ligand distance, thus producing a larger Stokes shift and broader optical bands.

Figure 12 shows the emission spectra of both polymorphs excited at 545 nm. Major peaks found around 597 nm are

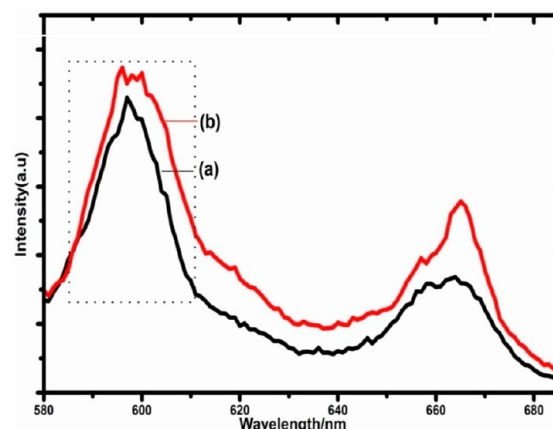


Figure 12. Emission spectra of (a)  $\alpha$ -KNdW<sub>2</sub>O<sub>8</sub> and (b)  $\beta$ -KNdW<sub>2</sub>O<sub>8</sub> excited at 545 nm.

responsible for transition from  $^4G_{5/2}$ ,  $^4G_{7/2}$  to the ground state of  $^4I_{9/2}$  corresponding to the orange emission. Spectra consists of another peak at 665 nm corresponding to the transition from  $^4F_{9/2}$  to the ground state, responsible for red emission. Careful observation of the peak centered at 597 nm as shown in Figure 12 indicates splits in the peak that could be further resolved. Splitting of the peak in  $\beta$ -KNdW<sub>2</sub>O<sub>8</sub> can be correlated with the strength of crystal field that arises from the difference in Nd–O bond distances in the monoclinic phase. As the Nd–O distance becomes shorter, it enhances the crystal field strength and thereby causes more splitting in the emission peaks. Moreover, as mentioned earlier, the considerable differences in the bond distances around Nd<sup>3+</sup> ions in  $\beta$ -KNdW<sub>2</sub>O<sub>8</sub> increases the crystal field strength and ultimately manifests itself as the split peak in photoluminescence spectra. Banski et al.<sup>37</sup> show that the crystal field of the material influences not only splitting of the peak but also the emission intensity from rare earth ions. According to Laporte's rule, 4f–4f electric dipole transitions in rare earth ions are forbidden. However, in the presence of host matrix, Laporte rules no longer apply. Therefore, photoluminescence intensity increases as the crystal field influences the 4f orbital of the Nd<sup>3+</sup> ion to overlap and cause the forbidden electric dipole transitions to become allowed.

Hence, we believe that the crystal field strength is also responsible for increased intensity of photoluminescence peaks in the monoclinic phase compared to the tetragonal phase. Inter atomic distances obtained from Rietveld refinement, PDF analysis, and further local environment information from Raman studies reveal the influence of the crystal structure on photoluminescence behavior.

#### 4. CONCLUSIONS

Solution combustion synthesis of the two polymorphs of KNdW<sub>2</sub>O<sub>8</sub> ( $\alpha$ -KNdW<sub>2</sub>O<sub>8</sub> and  $\beta$ -KNdW<sub>2</sub>O<sub>8</sub>) phosphors has been carried out and characterized by X-ray diffraction and SEM measurements. The detailed structural analysis using neutron Rietveld method, neutron PDF, and Raman measurements help explain the difference in the observed photoluminescent properties for both phases. Emission spectra

recorded for the first time in the visible region at two different excitation wavelengths show peaks in the blue region and red region, respectively. The broader bandwidth for  $\beta$ -KNdW<sub>2</sub>O<sub>8</sub> is correlated with a high degree of distortion in Nd–O polyhedra. This distortion also results in increased crystal field strength, contributing to the high intensity of photoluminescence peaks in comparison to the emission peaks of  $\alpha$ -KNdW<sub>2</sub>O<sub>8</sub>. It is apparent from the above study that these polymorphs can be utilized for light emitting applications since they show emission in the visible range.

## ■ ASSOCIATED CONTENT

### ■ Supporting Information

Figure 1. XRD pattern of (a)  $\alpha$ -KNdW<sub>2</sub>O<sub>8</sub> and (b)  $\beta$ -KNdW<sub>2</sub>O<sub>8</sub>. Table 1. Wave numbers and assignment of observed vibrational modes for  $\alpha$ -KNdW<sub>2</sub>O<sub>8</sub> and  $\beta$ -KNdW<sub>2</sub>O<sub>8</sub>. This information available free of charge via the Internet at <http://pubs.acs.org/>.

## ■ AUTHOR INFORMATION

### Corresponding Author

\*E-mail: [nalini@poornaprajna.org](mailto:nalini@poornaprajna.org).

### Notes

The authors declare no competing financial interest.

## ■ ACKNOWLEDGMENTS

S.S.M.B. thanks UGC, Government of India, for the award of a fellowship and is also thankful to Manipal University, India, for accepting this research as a part of a Ph.D. program. Research conducted at ORNL's Spallation Neutron Source was sponsored by the Scientific User Facilities Division, Office of Basic Energy Sciences, United States Department of Energy. S.S.M.B. and N.G.S. are thankful to Prof. Satish Patil, IISc, Bangalore, India, for providing the photoluminescence measurement facility. S.S.M.B. and N.G.S. thank CENSE, IISc, Bangalore, India, for SEM measurements.

## ■ REFERENCES

- (1) Chen, Y. F. *Appl. Phys. B: Lasers Opt.* **2004**, *78*, 685–687.
- (2) Mendioroz, A.; Balda, R.; Al-Saleh, M.; Fernández, J. *Opt. Mater.* **2005**, *27*, 1704–1710.
- (3) Jean Claude, G.; Eliseeva, S. V. *J. Rare Earth* **2010**, *28*, 824–842.
- (4) Klevtsov, P. V.; Kozeeva, L. P. *Sov. Phys. Crystallogr.* **1976**, *21*, 2–6.
- (5) Colon, C.; Alonso Medina, A.; Fernandez, F.; Saez Puche, R.; Volkov, V.; Cascales, C.; Zaldo, C. *Chem. Mater.* **2005**, *17*, 6635–6643.
- (6) Klevtsov, P. V.; Klevtsova, R. F. *J. Struct. Chem.* **1977**, *18*, 339–355.
- (7) Vaidyanathan, S.; Jeon, D. Y. *Int. J. Appl. Ceram. Technol.* **2009**, *6*, 453–458.
- (8) Kolesov, B. A.; Kozeeva, L. P. *J. Struct. Chem.* **1993**, *34*, 534–539.
- (9) Kato, A. N.; Uchitomi, S.; Oishi, S.; Shishido, T.; Iida, S. *Phys. Status Solidi C* **2006**, 2709–2712.
- (10) Qureshi, M.; Chen, H.; Lu, C. *Solid State Commun.* **2007**, *142*, 85–88.
- (11) Lee, G. H.; Kang, S. J. *Lumin.* **2011**, *131*, 2606–2611.
- (12) Qiong, W.; Donghua, C. *Opt. Laser. Technol.* **2009**, *41*, 783–787.
- (13) Guo, Y.; Sun, M.; Guo, W.; Ren, F.; Chen, D. *Opt. Laser. Technol.* **2010**, *42*, 1328–1331.
- (14) Amy, M.; Gindhart; Cora, L. *J. Mater. Res.* **2008**, *23* (1), 210–213.
- (15) Mukasyan, A. S.; Epstein, P.; Dinka, P. *Proc. Combust. Inst.* **2007**, *31* (2), 1789–1795.
- (16) Henglein, A. *Chem. Rev.* **1989**, *89*, 1861–1873.
- (17) Qian, X.; Pu, X.; Zhang, D.; Li, L.; Li, M.; Wu, S. J. *Lumin.* **2011**, *131*, 1692–1695.
- (18) Lou, X.; Chen, D. *Mater. Lett.* **2008**, *62*, 1681–1684.
- (19) Bin Im, W.; Page, K.; DenBaars, S. P.; Seshadri, R. *J. Mater. Chem.* **2009**, *19*, 8761–8766.
- (20) Sakak, K.; Terashita, N.; Kim, H.; Proffen, T.; Majzoub, E. H.; Tsunokake, S.; Nakamura, Y.; Akiba, E. *Inorg. Chem.* **2013**, *52*, 7010–7019.
- (21) Proffen, T.; Billinge, S. J.; Egami, L. T.; Louca, D. Z. *Kristallogr.* **2003**, *218*, 132–143.
- (22) Neufeld, J.; Feygenson, M.; Carruth, J.; Hoffmann, R.; Chipley, K. K. *Nuclear Instrum. Methods B* **2012**, *287*, 68–75.
- (23) Farrow, C. L.; Juhas, P.; Liu, J.; Bryndin, D.; Bozin, J.; Bloch, E. S.; Proffen, T.; Billinge, S. J. L. *J. Phys.: Condens. Matter.* **2007**, *19*, 335219.
- (24) Yi, H. C.; Varma, A.; Rogachev, A. S.; McGinn, P. J. *Ind. Eng. Chem. Res.* **1996**, *35*, 2982–2985.
- (25) Chen, D.; Zhang, B.; Zhuang, H.; Li, W.; Xu, S. *Mater. Lett.* **2002**, *57*, 399–402.
- (26) Xijuan, Y.; Pingbob, X.; Qingde, S. *Phys. Chem. Chem. Phys.* **2001**, *3*, 5266–5269.
- (27) Liu, G.; Li, J.; Chen, K. In *Advances in Ceramics - Synthesis and Characterization, Processing and Specific Applications*; Sikilidis, C., Ed.; InTech: Rijeka, Croatia, 2011; pp 49–74.
- (28) Larson, A. C.; Von Dreele, R. B. *Los Alamos National Laboratory Report LAUR*; Los Alamos National Laboratory: Los Alamos, NM, 2004; pp 86–748.
- (29) Macalik, L.; Deren, P. J.; Hanuza, J.; Strek, W.; Demidovich, A. A.; Kuzmin, A. N. *J. Mol. Struct.* **1998**, *450*, 179–192.
- (30) Asiri Naidu, S.; Boudin, S.; Varadaraju, U. V.; Raveau, B. J. *Solid State Chem.* **2011**, *184*, 2566–2570.
- (31) Kolesov, B. A.; Kozeeva, L. P. *J. Struct. Chem.* **1993**, *34*, 534–539.
- (32) Maczka, M. *J. Solid State Chem.* **1997**, *129*, 287–297.
- (33) Lemanski, K.; Gagor, A.; Kurnatowska, M.; Pazik, R.; Deren, P. J. *J. Solid State Chem.* **2011**, *184*, 2713–2718.
- (34) Liu, Y.; Kuang, J. *J. Lumin.* **2010**, *130*, 351–354.
- (35) Judd, R.; Loudon, R. *Proc. R. Soc. A* **1959**, *251*, 127–133.
- (36) Huang, J.; Xu, J.; Luo, H.; Yu, X.; Li, Y. *Inorg. Chem.* **2011**, *50*, 11487–11492.
- (37) Banski, M.; Podhorodecki, A.; Misiewicz, Z. *Mater. Sci.-Pol.* **2010**, *28*, 217–227.